

Quasiparticles governing the zero-temperature dynamics of the 1D spin-1/2 Heisenberg antiferromagnet in a magnetic field

Michael Karbach,¹ Daniel Biegel,¹ and Gerhard Müller²

¹ *Bergische Universität Wuppertal, Fachbereich Physik, D-42097 Wuppertal, Germany*

² *Department of Physics, University of Rhode Island, Kingston RI 02881-0817*

(Dated: February 1, 2008)

The $T = 0$ dynamical properties of the one-dimensional (1D) $s = \frac{1}{2}$ Heisenberg antiferromagnet in a uniform magnetic field are studied via Bethe ansatz for cyclic chains of N sites. The ground state at magnetization $0 < M_z < N/2$, which can be interpreted as a state with $2M_z$ spinons or as a state of M_z magnons, is reconfigured here as the vacuum for a different species of quasiparticles, the *psinons* and *antipsinons*. We investigate three kinds of quantum fluctuations, namely the spin fluctuations parallel and perpendicular to the direction of the applied magnetic field and the dimer fluctuations. The dynamically dominant excitation spectra are found to be sets of collective excitations composed of two quasiparticles excited from the psinon vacuum in different configurations. The Bethe ansatz provides a framework for (i) the characterization of the new quasiparticles in relation to the more familiar spinons and magnons, (ii) the calculation of spectral boundaries and densities of states for each continuum, (iii) the calculation of transition rates between the ground state and the dynamically dominant collective excitations, (iv) the prediction of lineshapes for dynamic structure factors relevant for experiments performed on a variety of quasi-1D antiferromagnetic compounds, including KCuF_3 , $\text{Cu}(\text{C}_4\text{H}_4\text{N}_2)(\text{NO}_3)_2$, and CuGeO_3 .

I. INTRODUCTION

Quantum spin chains are some of the most intensively studied models representing strongly fluctuating quantum many-body systems because of their amenability to exact analysis and because of the sustained interest in materials exhibiting quasi-one-dimensional magnetic properties. Of particular interest are the dynamical properties in the low-temperature regime, reflecting strong quantum fluctuations.

Quantum fluctuations result from the time evolution of nonstationary observables of a many-body system in the ground state. They can be investigated (experimentally, theoretically, or computationally) by dynamical probes. The three main ingredients of each dynamical probe, (i) interaction Hamiltonian, (ii) ground state, (iii) dynamical variable, make a specific set of collective excitations visible to the probe. The specificity is determined by the symmetries of all three ingredients.

A dynamical probe yields information on spectrum and transition rates. Different sets of data are collected from the same many-body system [ingredients (i) and (ii)] via particular fluctuation operators [ingredient (iii)]. Different views of the quantum fluctuations are filtered out by operator specific selection rules and transition rates.¹

Collective excitations are modes in which some of the tightly coupled fundamental degrees of freedom (electrons, ions, atoms) move collectively in more or less complex patterns. The free-particle like normal modes known to exist in systems made of linearly coupled degrees of freedom are the inspiration of attempts to describe collective excitations quite generally as composites of elementary modes that are weakly coupled at most. This requires that the ground state of the system can be meaningfully interpreted as a physical vacuum in which certain kinds of elementary excitations (quasiparticles)

move without attenuation and scatter off each other non-destructively.

In completely integrable many-body systems, the identity of the quasiparticles in any given eigenstate is upheld on a rigorous basis and encoded by a set of quantum numbers. All excited states can then indeed be generated systematically via the creation of quasiparticles from the ground state configured as a physical vacuum. The interaction of the quasiparticles may not be weak, but it is of a kind which preserves their identity. The factorizability of the associated S -matrices, which is characteristic of completely integrable systems, reduces all quasiparticle couplings to two-body scattering events for which a general solution can be formulated, e.g. in the form of a Bethe wave function.^{2,3}

The focus here is set on the quasiparticles which govern the quantum fluctuations of the one-dimensional (1D) $s = \frac{1}{2}$ Heisenberg antiferromagnet in an external magnetic field:^{4,5}

$$H = \sum_{n=1}^N [\mathbf{J}\mathbf{S}_n \cdot \mathbf{S}_{n+1} - hS_n^z]. \quad (1)$$

The ground state at $h \geq h_S = 2J$, $|F\rangle \equiv |\uparrow\uparrow \cdots \uparrow\rangle$, has saturated magnetization, $M_z = N/2$. It is the reference state of the coordinate Bethe ansatz and plays the role of the vacuum for *magnons* (spin-1 quasiparticles). All eigenstates of H are described as configurations of interacting magnons. The ground state at $h = 0$, $|A\rangle$, has magnetization $M_z = 0$. It contains $N/2$ magnons. In the framework of the Bethe ansatz, it is reconfigured as the physical vacuum for *spinons*, a species of spin- $\frac{1}{2}$ quasiparticles, and the entire spectrum of H is reinterpreted as composites of interacting spinon pairs. Likewise at intermediate fields, $0 < h < h_S$, the ground state $|G\rangle$ is reconfigured as a new physical vacuum, and the low-

lying collective excitations are most effectively described as composites of two new species of quasiparticles, named *psinon* and *antipsinon*.

In a recent paper,⁶ a detailed description of these quasiparticles in the framework of the coordinate Bethe ansatz was given. Their role in the zero-temperature spin fluctuations parallel to the direction of the magnetic field was elucidated in the form of lineshape predictions for the associated dynamic structure factor. Here we present a more comprehensive set of applications, which also includes the perpendicular spin fluctuations and the dimer fluctuations.

Physical realizations of Heisenberg antiferromagnetic chains have been known for many years in the form of 3D crystalline compounds with quasi-1D exchange coupling between magnetic ions. For the study of magnetic-field effects in the dynamics as predicted in this paper, the coupling must not be too weak or else it will be hard to reach the low-temperature regime. It must not be too strong either or else it will be hard to reach a magnetic field that makes the Zeeman energy comparable to the exchange energy. One compound that promises to be particularly suitable for this purpose is *copper pyrazine dinitrate* $[\text{Cu}(\text{C}_4\text{H}_4\text{N}_2)(\text{NO}_3)_2]$.⁷

The spin fluctuations can be observed directly via inelastic neutron scattering experiments. At very low temperatures, the dominant transitions in the scattering experiment are between the ground state $|G\rangle$ and a set of excitations $|\lambda\rangle$ that are reachable by one of the spin fluctuation operators $S_q^\mu = N^{-1/2} \sum_n e^{iqn} S_n^\mu$, $\mu = x, y, z$. In the $T = 0$ dynamic spin structure factors

$$S_{\mu\mu}(q, \omega) = 2\pi \sum_{\lambda} |\langle G | S_q^\mu | \lambda \rangle|^2 \delta(\omega - \omega_{\lambda}), \quad (2)$$

each transition with $\omega_{\lambda} \equiv E_{\lambda} - E_G$ and $q \equiv k_{\lambda} - k_G$ contributes a spectral line of intensity $2\pi |\langle G | S_q^\mu | \lambda \rangle|^2$.

Some quasi-1D antiferromagnetic compounds, of which CuGeO_3 is the most prominent example,^{8,9,10} are susceptible to a spin-Peierls transition, which involves a lattice distortion accompanied by an exchange dimerization. The dimer fluctuations, $D_q = N^{-1/2} \sum_n e^{iqn} \mathbf{S}_n \cdot \mathbf{S}_{n+1}$, as captured by the dynamic dimer structure factor

$$S_{DD}(q, \omega) = 2\pi \sum_{\lambda} |\langle G | D_q | \lambda \rangle|^2 \delta(\omega - \omega_{\lambda}) \quad (3)$$

may not be as directly observable as the spin fluctuations but an understanding of their quasiparticle composition is a matter of no less importance.

II. MAGNONS, SPINONS, PSINONS

The coordinate Bethe ansatz provides a natural classification of the eigenstates of (1) in terms of interacting magnons. The structure of the Bethe wave function, its determination via the solution of the Bethe ansatz equations, and its use for the calculation of matrix elements are summarized in the Appendix.

For our discussion here it turns out to be sufficient to consider r -magnon scattering states of the set K_r . In the invariant Hilbert subspace of magnetization $M_z = N/2 - r$, the Bethe quantum numbers of this set comprise, for $0 \leq r \leq N/2$ and $0 \leq m \leq N/2 - r$, all configurations

$$-\frac{r}{2} + \frac{1}{2} - m \leq I_1 < I_2 < \dots < I_r \leq \frac{r}{2} - \frac{1}{2} + m. \quad (4)$$

The Bethe ansatz suggests a threefold interpretation of the ground state $|G\rangle$ at $0 \leq M_z \leq N/2$ with quantum numbers

$$\{I_i\}_G = \left\{ -\frac{N}{4} + \frac{M_z}{2} + \frac{1}{2}, \dots, \frac{N}{4} - \frac{M_z}{2} - \frac{1}{2} \right\}. \quad (5)$$

Depending on the reference state (pseudo-vacuum) used, it can be regarded as a scattering state of $N/2 - M_z$ magnons, a scattering state of $2M_z$ spinons, or the physical vacuum of psinons.⁶

The states in the set K_r then all contain the same number of magnons or spinons but different numbers of psinons. The integer quantum number m selects all states from K_r that contain m pairs of psinons. The ground state $|G\rangle$ at $M_z = N/2 - r$ is the only state with $m = 0$. The quasiparticle role of the psinons in the 2-psinon ($m = 1$) and 4-psinon ($m = 2$) scattering states was highlighted previously.⁶

The excitations which are important in $S_{zz}(q, \omega)$ (parallel spin fluctuations) at $M_z = N/2 - r$ were found to consist of a small subset of K_r which includes $2m$ -psinon states over the entire range m . However, all $2m$ -psinon states with significant spectral weight were found to belong to particular configurations of Bethe quantum numbers I_i in which $2m - 1$ psinons behave like a single degree of freedom with properties akin to those attributed to an antiparticle. The spectrum of $S_{zz}(q, \omega)$ was thus identified as arising predominantly from psinon-antipsinon ($\psi\psi^*$) excitations.⁶ Here our goal is to identify and interpret the dynamically relevant excitations also for $S_{xx}(q, \omega) = \frac{1}{4}[S_{+-}(q, \omega) + S_{-+}(q, \omega)]$ (perpendicular spin fluctuations) and $S_{DD}(q, \omega)$ (dimer fluctuations), where we expect psinons and antipsinons to occur in different combinations.

III. SYMMETRIES AND CONSEQUENCES

Narrowing down the dynamically dominant sets of excitations and characterizing them as specific quasiparticle configurations proceeds in three steps. First we limit the set of relevant excitations by the application of selection rules which are imposed by the symmetry properties of the Hamiltonian (1) and the fluctuation operators S_q^z, S_q^\pm, D_q and which are valid for arbitrary system sizes. Then we identify additional selection rules that are valid only for $N \rightarrow \infty$. Finally, we identify from the states not yet excluded those whose transition rates are predominant in $S_{zz}(q, \omega)$, $S_{-+}(q, \omega)$, $S_{+-}(q, \omega)$, and $S_{DD}(q, \omega)$.

This last step, which here is carried out empirically, may very well find its ultimate justification by further symmetries related to complete integrability.¹¹

A. Selection rules for arbitrary N

The conservation laws of the total spin S_T and its z -component S_T^z imply that transitions between eigenstates of (1) induced by the (nonstationary) spin fluctuation operators S_q^z , S_q^\pm (vector) and the dimer fluctuation operator D_q (scalar) satisfy stringent selection rules. The six classes of excitations with permissible transitions from $|G\rangle$ with $S_T = S_T^z = M_z$ for the fluctuation operators S_q^z , S_q^\pm , D_q are all listed in Table I. The locations of these classes of excitations relative to the ground state in the (S_T, S_T^z) -plane are shown in Fig. 1.

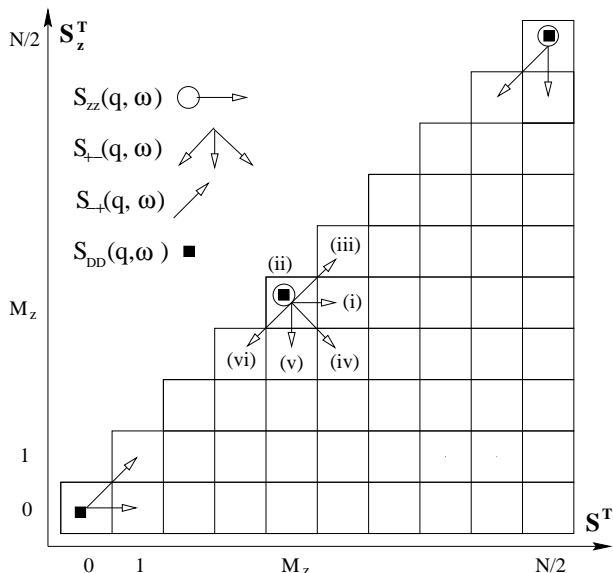


FIG. 1: Transitions between the ground state $|G\rangle$ with quantum numbers $S_T = S_T^z = M_z$ and six classes of excitations permitted by microscopic selection rules (Ref. 12). Each class may contribute to exactly one of three dynamic spin structure factors. Class (ii) also contributes to the dynamic dimer structure factor. Fewer classes of permissible excitations exist for $M_z = 0$ ($h = 0$) and $M_z = N/2$ ($h = h_S$).

We note that classes (ii), (iii), and (vi) include the sets K_r for $r = R, R-1, R+1$, respectively, while the remaining three classes (i), (iv), and (v) include sets of states that belong to the same S_T multiplets as the sets K_R or K_{R+1} . Table I also lists the Bethe quantum numbers $I_i, i = 1, \dots, r$ for the type- K_r or equivalent states and describes how the rapidities $z_i, i = 1, \dots, r$ for these states are obtained.

B. Selection rules for $N \rightarrow \infty$

Before we begin evaluating matrix elements from Bethe ansatz solutions in production mode, we take note that the rotational symmetry of the Hamiltonian (1) and the vector nature of the spin fluctuation operator (S_q^x, S_q^y, S_q^z) imply the following rigorous relations between transition rates involving excitations that belong to the same S_T -multiplet:¹²

$$|\langle G | S_q^z | \lambda^{(i)} \rangle|^2 = \frac{|\langle G | S_q^- | \lambda^{(iii)} \rangle|^2}{2(M_z + 1)}, \quad (6a)$$

$$|\langle G | S_q^+ | \lambda^{(iv)} \rangle|^2 = \frac{|\langle G | S_q^- | \lambda^{(iii)} \rangle|^2}{(M_z + 1)(2M_z + 1)}, \quad (6b)$$

$$|\langle G | S_q^+ | \lambda^{(v)} \rangle|^2 = \frac{2|\langle G | S_q^z | \lambda^{(ii)} \rangle|^2}{M_z}. \quad (6c)$$

The significance of the relations (6) is not limited to their usefulness in reducing computational work. The magnetization is an extensive quantity, implying $M_z \propto N$ at $h \neq 0$. All transition rates for class (i), (iv), (v) excitations are then suppressed by factors N or N^2 relative to the transition rates of class (ii), (iii) excitations. The consequence is that in a macroscopic system at $h \neq 0$, the spectral weight of all class (i), (iv), (v) excitations in the $T = 0$ dynamic spin structure factors $S_{\mu\mu}(q, \omega)$ is negligible.¹³

C. Selection rules related to integrability

We shall find empirically that in each one of the remaining classes (ii), (iii), and (vi) there exists a two-parameter set of excitations which governs one of the dynamic structure factors of interest here. We shall name these sets P2, P3, and P6, respectively (see Table I). Corresponding finite- N spectral contributions of class (i), (iv), and (v) states can be inferred from Eqs. (6). The associated sets P1, P4, and P5 have their position in the (q, ω) -plane shifted vertically relative to the sets P2, P3, and P6 because of the Zeeman splitting, and the spectral weight of the former is suppressed by factors N or N^2 as explained previously.

IV. DYNAMICALLY DOMINANT EXCITATIONS

In our search for the dynamically most relevant excitations, we focus on the case of magnetization $M_z/N = \frac{1}{4}$ (half the saturation value). We explore the transition rates for the spin and dimer fluctuation operators between the ground state $|G\rangle$ and the type- K_r states in the classes (ii), (iii), (vi). These excitations are found to contribute most of the spectral weight to the dynamic spin and dimer structure factors.

TABLE I: Specifications of type- K_r or equivalent states from six classes. Each class contains states that contribute to a specific dynamic spin structure factor at $T = 0$. Class (ii) also contributes to the dynamic dimer structure factor. All specifications are relative to a given ground state with $S_T^z = S_T = N/2 - R = M_z$, where M_z is the magnetization in a field of a certain strength h . The last column identifies the three subsets of excitations which dominate the spin and dimer fluctuations for $N \rightarrow \infty$.

class	S_T S_T^z	$S_{\mu\mu}(q, \omega)$	r	Bethe quantum numbers	Bethe ansatz solutions	dynamically dominant sets
(i)	$M_z + 1$ M_z	$S_{zz}(q, \omega)$	R	$I_i^{(i)} = I_i^{(iii)} + \frac{1}{2}, i = 1, \dots, R-1$ $I_R^{(i)} = \frac{1}{2}(N - R + 1)$	$z_i^{(i)} = z_i^{(iii)}, i = 1, \dots, R-1$ $z_R^{(i)} = \infty$	
(ii)	M_z M_z	$S_{zz}(q, \omega)$ $S_{DD}(q, \omega)$	R	$I_i^{(ii)}, i = 1, \dots, R$ from (4) with $r = R$	$z_i^{(ii)}, i = 1, \dots, R$ from (A3) with $r = R$	$\psi\psi^*$ (P2)
(iii)	$M_z + 1$ $M_z + 1$	$S_{-+}(q, \omega)$	$R-1$	$I_i^{(iii)}, i = 1, \dots, R-1$ from (4) with $r = R-1$	$z_i^{(iii)}, i = 1, \dots, R-1$ from (A3) with $r = R-1$	$\psi\psi$ (P3)
(iv)	$M_z + 1$ $M_z - 1$	$S_{+-}(q, \omega)$	$R+1$	$I_i^{(iv)} = I_i^{(iii)} + 1, i = 1, \dots, R-1$ $I_R^{(iv)} = I_{R+1}^{(iv)} = \frac{1}{2}(N - R)$	$z_i^{(iv)} = z_i^{(iii)}, i = 1, \dots, R-1$ $z_R^{(iv)} = z_{R+1}^{(iv)} = \infty$	
(v)	M_z $M_z - 1$	$S_{+-}(q, \omega)$	$R+1$	$I_i^{(v)} = I_i^{(ii)} + \frac{1}{2}, i = 1, \dots, R$ $I_{R+1}^{(v)} = \frac{1}{2}(N - R)$	$z_i^{(v)} = z_i^{(ii)}, i = 1, \dots, R$ $z_{R+1}^{(v)} = \infty$	
(vi)	$M_z - 1$ $M_z - 1$	$S_{+-}(q, \omega)$	$R+1$	$I_i^{(vi)}, i = 1, \dots, R+1$ from (4) with $r = R+1$	$z_i^{(vi)}, i = 1, \dots, R+1$ from (A3) with $r = R+1$	$\psi\psi^*$ (P6)

A. Perpendicular spin fluctuations (P3)

The spectral weight in $S_{-+}(q, \omega)$ is carried exclusively by class (iii) excitations (see Table I). A systematic study of the transition rates of type- K_{R-1} states for $m = 0, 1, 2, \dots$ reveals that the dominant contributions to the spectral weight come from two-psinon ($\psi\psi$) states. The Bethe quantum numbers of the states involved in these transitions are shown in Fig. 2 for $N = 16$ and $M_z = 4$. The top row represents the ground state $|G\rangle$, which contains four magnons (small circles) or eight spinons (large circles). This is the psinon vacuum at $R = 4$. The next row is the lowest-lying two-psinon ($\psi\psi$) state excited from $|G\rangle$. This excitation also plays the role of the psinon vacuum ($m = 0$) at $R = 3$. It is then characterized as containing three magnons or ten spinons.

Mobilizing the two innermost spinons turns them into psinons (gray circles). The remaining five rows in Fig. 2 represent $\psi\psi$ states ($m = 1$) at $0 < q \leq \pi$ for $R = 3$. The state in the second row is also counted as a $\psi\psi$ state. Hence there are six of them in total for $N = 16$. Freeing up two additional spinons from the sidelines produces a set of four-psinon states ($m = 2$) of which the $\psi\psi$ states ($m = 0, 1$) are special members. The maximum number of psinons that can be mobilized at $R = 3$ is equal to the number of spinons: $2M_z = 10$.

We have calculated the transition rates $|\langle G | S_q^- | \lambda^{(iii)} \rangle|^2$ between the ground state for $N = 24$, $M_z = 4$ and all $2m$ -psinon excitations. We found that the $\psi\psi$ states are predominant. They are listed in Table II along with the momentum and energy transfer of the associated spectral lines. For $N \rightarrow \infty$ the $\psi\psi$ states form the continuum P3 in (q, ω) -space. In Fig. 3(a) we have plotted all states belonging to P3 for $N = 64$ (circles) and the spectral boundaries for $N \rightarrow \infty$. The range of P3 is restricted to

$\bar{q}_s \leq |q| \leq \pi$, where

$$\bar{q}_s \equiv 2\pi M_z / N. \quad (7)$$

Note that the continuum P3 is displaced by $\Delta q = \pi$ relative to the two-psinon continuum discussed in the context of Ref. 6. The psinon vacuum used for P3 is the state in the first row of Fig. 2. In Ref. 6 the state in the second row is the vacuum. These choices are dictated by the different fluctuation operators considered now and then.

The relative integrated intensity of the $\psi\psi$ states, $S_{-+}^{\psi\psi}(q)/S_{-+}(q)$, is plotted in Fig. 3(b) for various N at fixed $M_z = N/4$. Corresponding data for the absolute integrated intensity $S_{-+}(q)$ are shown in the inset. We observe that there is virtually no intensity at $|q| \leq \bar{q}_s$, outside the range of continuum P3. As $|q|$ increases from q_s toward π , $S_{-+}(q)$ increases gradually and at an accelerated rate. The value at the zone boundary diverges

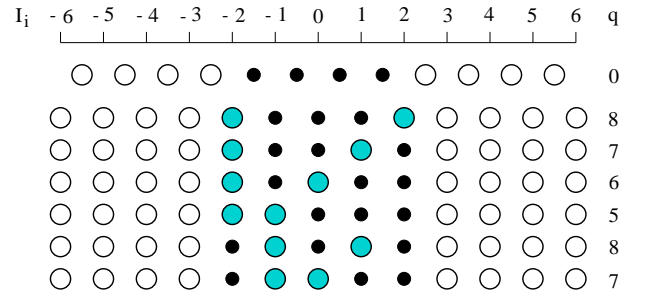


FIG. 2: Psinon vacuum $|G\rangle$ for $N = 16$, $M_z = 4$ and $\psi\psi$ states with $q \geq 0$ from the set K_3 out of class (iii). The I_i values are marked by the positions of the magnons (small circles). The spinons (large circles) mark I_i -vacancies. A subset of the spinons are called psinons (gray circles). The wave numbers $q \equiv k - k_G$ are given in units of $2\pi/N$.

TABLE II: $\psi\psi$ states with $q \equiv k - k_G \geq 0$ from the set K_{R-1} out of class (iii) excited from the psinon vacuum $|G\rangle$ for $N = 24$, $R = 6$: Bethe quantum numbers, wave number (in units of $2\pi/N$), energy, and transition rate. The ground state has $k_G = 0$ and $E_G = -11.5121346862$ and is realized at $h = 1.58486 \dots$ for $N \rightarrow \infty$.

$2I_i$	q	$E - E_G + h$	$ \langle G S_q^- \lambda^{(iii)}\rangle ^2$
-2 +0 +2 +4 +6	7	1.8184194057	0.0626472812
-4 +0 +2 +4 +6	8	1.9556536638	0.1424479327
-4 -2 +2 +4 +6	9	2.0088932004	0.2414561733
-4 -2 +0 +4 +6	10	1.9746665911	0.3895105465
-4 -2 +0 +2 +6	11	1.8556790610	0.6950450037
-4 -2 +0 +2 +4	12	1.6606927007	2.2311978057
-6 +0 +2 +4 +6	9	2.1612403300	0.0104636629
-6 -2 +2 +4 +6	10	2.2113923024	0.0348248694
-6 -2 +0 +4 +6	11	2.1742818977	0.0780182561
-6 -2 +0 +2 +6	12	2.0527517142	0.1743614335
-6 -4 +2 +4 +6	11	2.3389550993	0.0062315774
-6 -4 +0 +4 +6	12	2.2987048423	0.0260883689

in the thermodynamic limit: $S_{-+}(\pi) \sim N^{1-1/\eta}$, with an exponent $\eta(M_z/N)$ that assumes the value^{14,15}

$$\eta(1/4) = 1.53122 \dots \quad (8)$$

for the situation at hand. It reflects the divergence $S_{-+}(q) \sim |\pi - q|^{1/\eta-1}$ for $N = \infty$. The relative $\psi\psi$ contribution to $S_{-+}(q)$ rises rapidly from zero at $q \gtrsim q_s$ toward a value exceeding 97.8% at $q = \pi$. The solid line in the inset is obtained from a two-parameter fit, $a|\pi - q|^{1/\eta-1} + b$, of the data at $q \geq \pi/2$.

When we decrease M_z at fixed N , the soft mode at $q = \pi$ remains stationary while the soft mode at $q = \bar{q}_s$

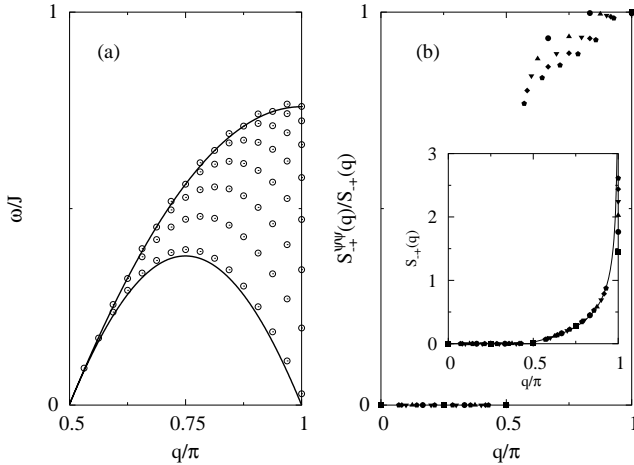


FIG. 3: (a) Energy versus wave number of the $\psi\psi$ excitations at $M_z = N/4$ for $N = 64$ (circles) and $N \rightarrow \infty$ (continuum P3 between curves). (b) Integrated intensity of $S_{-+}(q)$ (inset) and relative $\psi\psi$ contribution (main plot) for $N = 12, 16, 20, 24, 28$.

moves to the left. At $M_z = 0$, the $\psi\psi$ states become the two-spinon triplets. The two-spinon part of $S_{-+}(q, \omega)$ is exactly known for $N \rightarrow \infty$.^{16,17} Conversely, when we increase M_z , the soft mode at $q = \bar{q}_s$ moves to the right and thus narrows the range of P3 continually. At saturation ($M_z/N = \frac{1}{2}$) the function $S_{-+}(q, \omega)$ vanishes identically.

B. Dimer and parallel spin fluctuations (P2)

The parallel spin fluctuations were already analyzed in Ref. 6. The relevant excitations are contained in the set K_R out of class (ii). This set is subdivided into sets of $2m$ -psinon states for $0 \leq m \leq M_z = N/2 - R$. Each set for $m > 0$ contributes one branch of excitations with significant spectral weight to $S_{zz}(q, \omega)$. Figure 4 shows the configurations of Bethe quantum numbers I_i of all these states for $N = 16$, $M_z = 4$. The top row represents the psinon vacuum ($m = 0$). The four groups of states underneath represent the dynamically dominant branches of $2m$ -psinon states for $m = 1, \dots, 4$.

We argued that the I_i -configurations of these excitations suggest a simpler interpretation in terms of two quasiparticles, namely one psinon (ψ) and one antipsinon (ψ^*). We reinterpreted the series of dynamically dominant branches taken from $2m$ -parameter sets of multiple-psinon states as a single two-parameter set of $\psi\psi^*$ scattering states. These states form the continuum P2 for

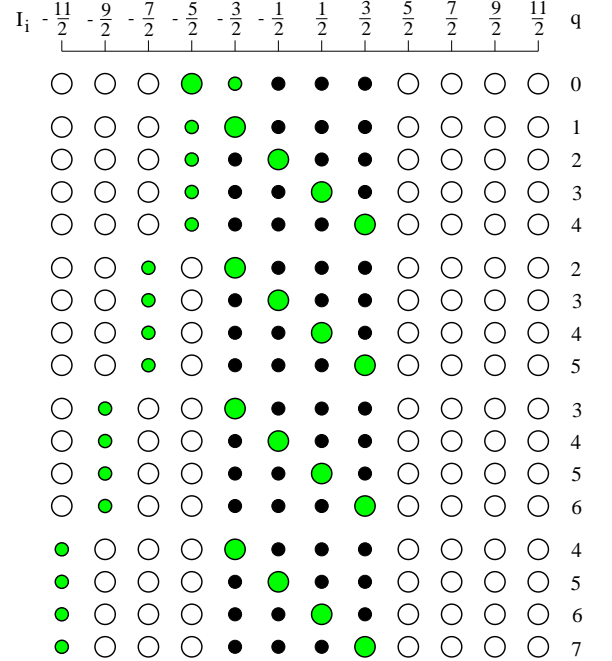


FIG. 4: Psinon vacuum $|G\rangle$ for $N = 16$, $M_z = 4$ and set of $\psi\psi^*$ states with $0 \leq q \leq \pi$ out of the set K_4 . The I_i are given by the positions of the magnons (small circles) in each row. The spinons (large circles) correspond to I_i -vacancies. The psinon (ψ) and the antipsinon (ψ^*) are marked by a large and a small grey circle, respectively.

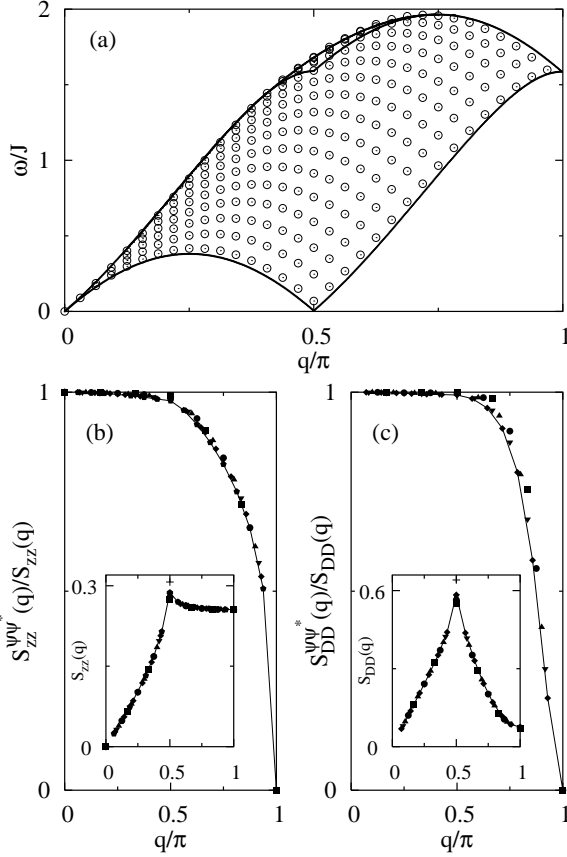


FIG. 5: (a) Energy versus wave number the $\psi\psi^*$ excitations at $M_z/N = 1/4$ for $N = 64$ (circles) and $N \rightarrow \infty$ (partially folded continuum P2 outlined by solid lines). (b) Integrated intensity $S_{zz}(q)$ (inset) and relative P2 contribution (main plot) for $N = 12, 16, 20, 24, 28, 32$. (c) Integrated intensity $S_{DD}(q)$ (inset) and relative P2 contribution (main plot) for $N = 12, 16, 20, 24, 28$. The lines in (b) connect the $N = 32$ data points and the lines in (c) the $N = 28$ data points. The values of $S_{zz}(\pi/2)$ and $S_{DD}(\pi/2)$ extrapolated to $N \rightarrow \infty$ are marked (+).

$N \rightarrow \infty$ in the (q, ω) -plane as illustrated in Fig. 5(a). From the shape of the continuum with its soft modes at $q = 0$ and $q = q_s$, where

$$q_s \equiv \pi - 2\pi M_z/N, \quad (9)$$

and with the partial overlap along a stretch of the upper boundary, we reconstructed the energy-momentum relations of the ψ and ψ^* quasiparticles.⁶

The corresponding search for the dynamically dominant dimer excitations again points to the $\psi\psi^*$ continuum P2. The $\psi\psi^*$ transition rates for the fluctuation operators S_q^z and D_q in a system with $N = 16$, $M_z = 4$ are listed in Table III for comparison. These data suggest that the spectral weight in $S_{DD}(q, \omega)$ is concentrated more heavily at lower energy than is observed in $S_{zz}(q, \omega)$. A more quantitative discussion of this evidence will follow in Sec. V.

TABLE III: $\psi\psi^*$ states with $q \equiv k - k_G \geq 0$ from the set K_R out of class (ii) excited from the psinon vacuum $|G\rangle$ for $N = 16$, $R = 4$: quantum number m , wave number (in units of $2\pi/N$), energy, and transition rates. The ground state has $k_G = 0$ and $E_G = -11.5121346862$ and is realized at $h = 1.58486 \dots$ for $N \rightarrow \infty$. The Bethe quantum numbers were listed in Table II of Ref. 6.

$2m$	q	$E - E_G$	$ \langle G S_q^z \lambda^{(ii)} \rangle ^2$	$ \langle G D_q \lambda^{(ii)} \rangle ^2$
0	0	0.0000000000	1.0000000000	1.0000000000
2	1	0.3504534152	0.0484825989	0.1201967890
2	2	0.5271937189	0.0587154211	0.1687346681
2	3	0.5002699273	0.0773592284	0.2298023543
2	4	0.2722787522	0.1257902349	0.3456324084
4	2	0.7981588810	0.0426892576	0.0720507048
4	3	0.9653287066	0.0552255878	0.1098585317
4	4	0.9301340415	0.0743667351	0.1555227849
4	5	0.6966798553	0.1253357676	0.2470269183
6	3	1.2708459328	0.0345439774	0.0307838904
6	4	1.4285177129	0.0516860817	0.0553527352
6	5	1.3858078992	0.0753564030	0.0866741700
6	6	1.1488426600	0.1406415212	0.1563073306
8	4	1.6819046570	0.0235815843	0.0060903835
8	5	1.8257803105	0.0443726010	0.0140423747
8	6	1.7724601200	0.0744641955	0.0259881320
8	7	1.5309413164	0.1686893882	0.0589091070

Finite- N data for the integrated intensities $S_{zz}(q)$ and $S_{DD}(q)$ are presented in Figs. 5(b) and (c), respectively. Both static structure factors rise from zero at $q = 0$ to a cusp-like maximum at $q = q_s = \pi/2$, where the soft mode is located. The cusp is of the form $\sim |q_s - q|^{\eta-1}$. A two-parameter fit, $aN^{1-\eta} + b$, of the data at $q = q_s$ yields the extrapolated values $S_{zz}(\pi/2) \simeq 0.307$ and $S_{DD}(\pi/2) \simeq 0.641$. On approach to $q = \pi$, the intensity drops more drastically in $S_{DD}(q)$ than in $S_{zz}(q)$.

For both kinds of fluctuations, the intensity at $q \leq q_s$ is almost exclusively originating from $\psi\psi^*$ excitations. At $q = q_s$, the relative $\psi\psi^*$ contributions to $S_{zz}(q)$ and $S_{DD}(q)$ are estimated to be at least 93% and 95%, respectively, in the limit $N \rightarrow \infty$. At $q \gtrsim q_s$ the $\psi\psi^*$ parts of $S_{zz}(q)$ and $S_{DD}(q)$ decrease monotonically but remain dominant except in the immediate vicinity of the zone boundary. The data suggest a qualitative difference in how the relative $\psi\psi^*$ intensities approach zero as $q \rightarrow \pi$. If the behavior near the zone boundary can be described by a power-law, $\sim |\pi - q|^\gamma$, then we predict $\gamma \gtrsim 1$ for the dimer fluctuations and $\gamma \simeq 0.3$ for the spin fluctuations.⁶

Upon varying the value of M_z , the continuum P2 changes its shape continuously. In both limits, $M_z/N \rightarrow 0$ and $M_z/N \rightarrow \frac{1}{2}$, it degenerates into a single branch and then vanishes.^{6,12} At $M_z = 0$ the dimer fluctuations and the spin fluctuations are produced by entirely different sets of excitations. $S_{zz}(q, \omega)$ is known to be dominated by the continuum of two-spinon triplet

excitations,¹⁶ which are Bethe ansatz solutions with real rapidities. $S_{DD}(q, \omega)$ is presumably governed by two-spinon singlet excitations, which are Bethe ansatz solutions with complex rapidities.¹⁸

C. Perpendicular spin fluctuations (P6)

For finite N , the spectral weight in the dynamic structure factor $S_{+-}(q, \omega)$ probes excitations from classes (iv)-(vi). However, we know from Sec. IIIB that the intensities of class-(iv) and class-(v) excitations are bound to fade away in the limit $N \rightarrow \infty$. The class-(vi) excitations contain the set K_{R+1} . It turns out that much of the spectral weight in $S_{+-}(q, \omega)$ is carried again by $\psi\psi^*$ excitations. However, the transitions $\langle G|S_q^+|\lambda \rangle$ probe the $\psi\psi^*$ states in a different invariant subspace than the transitions $\langle G|S_q^z|\lambda \rangle$, $\langle G|D_q|\lambda \rangle$ do. This causes some dramatic changes in the spectrum and in the spectral-weight distribution.

The differences are best illustrated by Fig. 6 in relation to Figs. 2 and 4. The top row in all three figures shows the I_i -configuration of the ground state $|G\rangle$ for $N = 16$, $M_z = 4$. The remaining rows in Fig. 4 represent the $\psi\psi^*$ states in the same invariant subspace, whereas the

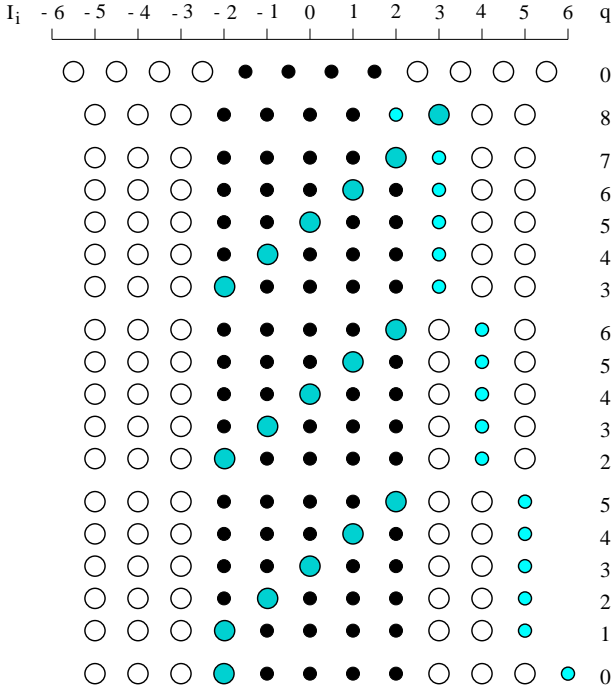


FIG. 6: Psinon vacuum $|G\rangle$ for $N = 16$, $M_z = 4$ and set of $\psi\psi^*$ states with $0 \leq q \leq \pi$ out of the set K_5 . The I_i are given by the positions of the magnons (small circles) in each row. The spinons (large circles) correspond to I_i -vacancies. The psinon (ψ) and the antipsinon (ψ^*) are marked by a large and a small grey circle, respectively. The last row describe a state from class (v) which belongs to the same S_T -multiplet as the psinon vacuum.

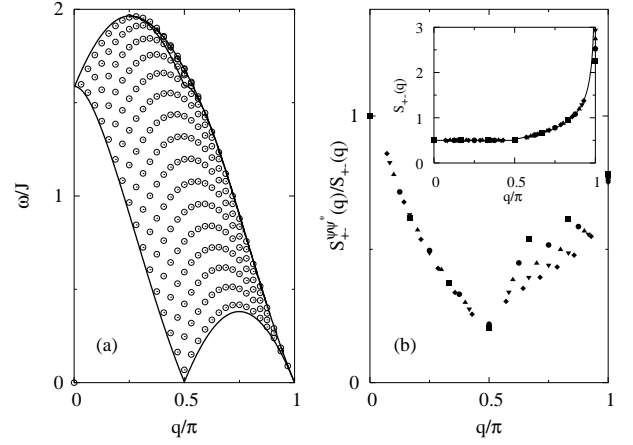


FIG. 7: (a) Energy versus wave number the $\psi\psi^*$ excitations at $M_z = N/4$ for $N = 64$ (circles) and $N \rightarrow \infty$ (partially folded continuum P6 outlined by solid lines). (b) Integrated intensity $S_{+-}(q)$ (inset) and relative P6 contribution (main plot) for $N = 12, 16, 20, 24, 28$. The solid line in the inset results from a two-parameter fit as explained in the context of Fig. 3.

remaining rows in Fig. 2 represent the $\psi\psi$ states in the subspace with one less magnon (i.e. two more spinons). The first $\psi\psi$ state (second row in Fig. 2) also plays the role of the psinon vacuum in that subspace.

The second row in Fig. 6 represents the lowest excitation probed by $\langle G|S_q^+|\lambda \rangle$ and, at the same time, the psinon vacuum with one more magnon (i.e. two less spinons). The three groups of five states underneath represent the complete set of $\psi\psi^*$ states in the same invariant subspace. Because the momentum transfer for these $\psi\psi^*$ states is relative to a different psinon vacuum than was the case for the $\psi\psi^*$ states discussed in Fig. 4, the observable spectrum of the continuum P6 which emerges for $N \rightarrow \infty$ [Fig. 7(a)] is the mirror image of the continuum P2 [Fig. 5(a)].

The last row in Fig. 6 is not exactly a $\psi\psi^*$ state. It differs from the $\psi\psi^*$ in the previous row only by the smallest change in one Bethe quantum number. This class-(v) state belongs to the same S_T -multiplet as the ground state $|G\rangle$ (top row). We have included it here because its transition rate is significant. In fact, it is the only excitation at $q = 0$ with a nonzero transition rate. Even though it is not a member of the set K_{R+1} , its contribution to $S_{+-}(q, \omega)$ marks a natural endpoint of the continuum P6. The excitation energies and transition rates pertaining to all states shown in Fig. 6 are listed in Table IV.

The integrated intensity $S_{+-}(q)$ as shown in Fig. 7(b) is almost flat in the region $0 \leq q \leq q_s$. The intensity at $q = 0$ is exactly known:¹²

$$S_{+-}(0) = 2M_z/N = 1/2. \quad (10)$$

At $q > \bar{q}_s$ the function $S_{+-}(q)$ rises gradually and with increasing slope ending in a divergence at $q = \pi$. The

TABLE IV: $\psi\psi$ states with $q \equiv k - k_G \geq 0$ from the set K_{R+1} out of class (vi) excited from the spinon vacuum $|G\rangle$ for $N = 16$, $R = 4$: Bethe quantum numbers, quantum number m , wave number (in units of $2\pi/N$), energy, and transition rate. The ground state has $k_G = 0$ and $E_G = -11.5121346862$ and is realized at $h = 1.58486\dots$ for $N \rightarrow \infty$. The last row describe a state from class (v) which belongs to the same S_T -multiplet as $|G\rangle$.

$2I_i$	$2m$	q	$E - E_G - h$	$ \langle G S_q^+ \lambda^{(vi)}\rangle ^2$
-4 - 2 + 0 + 2 + 4	0	8	-1.4624484093	1.9420228564
-4 - 2 + 0 + 2 + 6	2	7	-1.0239463125	0.6324984574
-4 - 2 + 0 + 4 + 6	2	6	-0.7427954774	0.0473348211
-4 - 2 + 2 + 4 + 6	2	5	-0.6661027722	0.0187604165
-4 + 0 + 2 + 4 + 6	2	4	-0.8076063179	0.0156977974
-2 + 0 + 2 + 4 + 6	4	3	-1.1468483618	0.0980201222
-4 - 2 + 0 + 2 + 8	4	6	-0.5201660070	0.3553105587
-4 - 2 + 0 + 4 + 8	4	5	-0.2494575408	0.0606512819
-4 - 2 + 2 + 4 + 8	4	4	-0.1822770670	0.0309111714
-4 + 0 + 2 + 4 + 8	6	3	-0.3302018783	0.0280474732
-2 + 0 + 2 + 4 + 8	6	2	-0.6710449481	0.2106074048
-4 - 2 + 0 + 2 + 10	6	5	-0.0400322092	0.1984683911
-4 - 2 + 0 + 4 + 10	6	4	+0.2167505272	0.0646015620
-4 - 2 + 2 + 4 + 10	8	3	+0.2717353551	0.0401817835
-4 + 0 + 2 + 4 + 10	8	2	+0.1166329921	0.0372990435
-2 + 0 + 2 + 4 + 10	8	1	-0.2237883038	0.3577163008
-4 - 2 + 0 + 2 + 12	8	0	0.0000000000	0.5000000000

relation

$$S_{+-}(q) = 2M_z/N + S_{-+}(q) \quad (11)$$

dictates that the singularity is the one already described in Sec. IV A: $S_{+-}(q) \sim |\pi - q|^{1/\eta-1}$.

The relative $\psi\psi^*$ contribution to the integrated intensity is largest near the zone center and near the zone boundary as shown in the inset to Fig. 7(b). It gradually drops from 100% at $q = 0$ to $\sim 20\%$ at the soft-mode position $q = \bar{q}_s$ and then rises back to $\sim 72.5\%$ at $q = \pi$. Note that the N -dependence of the relative intensity data is much stronger at $q > \bar{q}_s$ than at $q \leq \bar{q}_s$. We shall see that the qualitatively different N -dependences are also observed in transition rates, from which interesting conclusions can be drawn.

V. LINESHAPES

To calculate the lineshapes of the $\psi\psi$ and $\psi\psi^*$ contributions to the dynamic spin and dimer structure factors we use, wherever applicable, the product ansatz

$$S(q, \omega) = D(q, \omega)M(q, \omega) \quad (12)$$

discussed at some length in Ref. 6. The factor $D(q, \omega)$ is the density of $\psi\psi$ or $\psi\psi^*$ states, which can be evaluated

for very large N via Bethe ansatz. The factor $M(q, \omega)$ represents the scaled transition rates $N|\langle G|S_q^\mu|\lambda\rangle|^2$, $\mu = z, +, -$, or $N|\langle G|D_q|\lambda\rangle|^2$ between the ground state and the sets of $\psi\psi$ or $\psi\psi^*$ states. These matrix elements are also calculated via Bethe ansatz but only for much smaller systems.

For the applications considered here, the product ansatz depends on a reasonably fast convergence, within the spectral boundaries of the continua P2, P3, and P6, of the finite- N transition rate data toward a smooth function $M(q, \omega)$ as $N \rightarrow \infty$. Problems with this ansatz arise when the finite-size excitations for which transition rates are available are subject to significant energy shifts caused by the quasiparticle interaction. For $\psi\psi$ and $\psi\psi^*$ scattering states, these are effects of $O(N^{-1})$ as discussed in Ref. 6. The exercise of caution is also indicated when the scaling behavior of the finite-size transition rates changes at spectral boundaries as is frequently the case.

Notwithstanding these caveats, the product ansatz is a useful tool for merging the best available transition-rate data and density-of-states data. It was successfully tested for the two-spinon excitations at $M_z = 0$.¹⁶ Any major distortions of the lineshapes predicted by the product ansatz can be avoided if we omit all data points of $M(q, \omega)$ that are shifted across spectral boundaries. Any theoretical and computational advances that make it possible to calculate transition rates for larger systems will improve the predictive power of the product ansatz.

A. $S_{DD}(q, \omega)$ and $S_{zz}(q, \omega)$

What can be observed in a fixed- q scan of the dimer and parallel spin fluctuations at $q = q_s$? The lineshape determination of $S_{DD}^{\psi\psi^*}(\pi/2, \omega)$ is illustrated in Fig. 8 in comparison with corresponding data for $S_{zz}^{\psi\psi^*}(\pi/2, \omega)$ as shown in Fig. 8 of Ref. 6. The first factor in the product ansatz is the same for both sets of data, namely the density of $\psi\psi^*$ states in continuum P2. It has the characteristic shape with a square-root divergence at the upper band edge ω_U as shown in panel (a).

The scaled transition rates $M_{zz}^{\psi\psi^*}(\pi/2, \omega)$ and $M_{DD}^{\psi\psi^*}(\pi/2, \omega)$ [panel (b)] are monotonically decreasing functions. For both kinds of fluctuations the data at low frequencies are consistent with the power-law divergence,

$$S_{zz}^{\psi\psi^*}(\pi/2, \omega) \sim S_{DD}^{\psi\psi^*}(\pi/2, \omega) \sim \omega^{\eta-2} \quad (13)$$

with $\eta - 2 = -0.468\dots$ as predicted by conformal invariance. It is near ω_U where the two sets of data differ most. While both transition rate functions tend to vanish at ω_U , this tendency is considerably slower for the parallel spin fluctuations than for the dimer fluctuations. The resulting lineshapes are dramatically different.

We saw that the slow approach to zero at ω_U of the parallel spin transition rates $M_{zz}^{\psi\psi^*}(\pi/2, \omega)$ combined with the divergence in $D^{\psi\psi^*}(\pi/2, \omega)$ produces a diverging

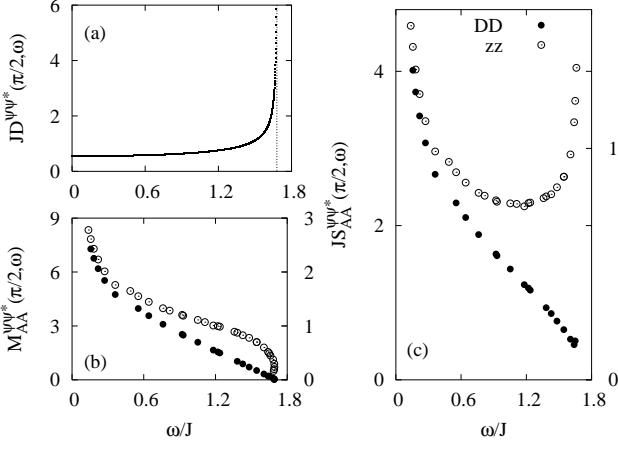


FIG. 8: (a) Density of $\psi\psi^*$ states at $q = \pi/2$ for $N = 2048$. (b) Dimer (DD) and parallel spin (zz) transition rates between the psinon vacuum and the $\psi\psi^*$ states at $q = \pi/2$ for $N \leq 32$ (zz) and $N \leq 28$ (DD). (c) Lineshape at $q = \pi/2$ of the $\psi\psi^*$ contribution to $S_{zz}(q, \omega)$ and $S_{DD}(q, \omega)$. All results are for $M_z = N/4$. The scales in (b) and (c) on the left (right) are for DD (zz).

trend at ω_U in $S_{zz}^{\psi\psi^*}(\pi/2, \omega)$. The result is a characteristic double-peak structure.⁶ The more rapid approach to zero of the dimer transition rates $M_{DD}^{\psi\psi^*}(\pi/2, \omega)$ overcomes the divergence of $D^{\psi\psi^*}(\pi/2, \omega)$ and produces a single-peak lineshape in $S_{DD}^{\psi\psi^*}(\pi/2, \omega)$.

Now we consider the wave numbers halfway between the soft mode q_s and the zone boundary or the zone center. The lineshape determination via product ansatz of $S_{DD}^{\psi\psi^*}(q, \omega)$ at $q = \pi/4, 3\pi/4$ is illustrated in Fig. 9. The corresponding data for the parallel spin fluctuations were shown in Fig. 9 of Ref. 6. For this situation the upper edge of one band ($q = \pi/4$) coincides with the lower edge of the other band ($q = 3\pi/4$).

Even though the number of available data points for dimer transition rates is limited, there is a clear indication that the lineshapes of the dimer fluctuations again consist of single-peak structures with a divergence at the lower band edge $\omega_L \neq 0$ and a shoulder reaching to the upper band edge ω_U , in strong contrast to the double-peak structures predicted for the lineshapes of the parallel spin fluctuations.

In summary, the spectral-weight distribution of the dynamic structure factors which probe the dimer and parallel spin fluctuations have many commonalities but also some very distinct properties. In both cases, the dominant spectrum is the continuum P2 of $\psi\psi^*$ states within the invariant M_z subspace which also contains the ground state $|G\rangle$. Both functions $S_{DD}^{\psi\psi^*}(q, \omega)$ and $S_{zz}^{\psi\psi^*}(q, \omega)$ are strongly peaked along the lower continuum boundary $\omega_L(q)$. Only the latter is also peaked along the upper continuum boundary $\omega_U(q)$. The divergence along $\omega_L(q)$ is caused by the transition rates, whereas the divergence along $\omega_U(q)$ is a density-of-states effect.

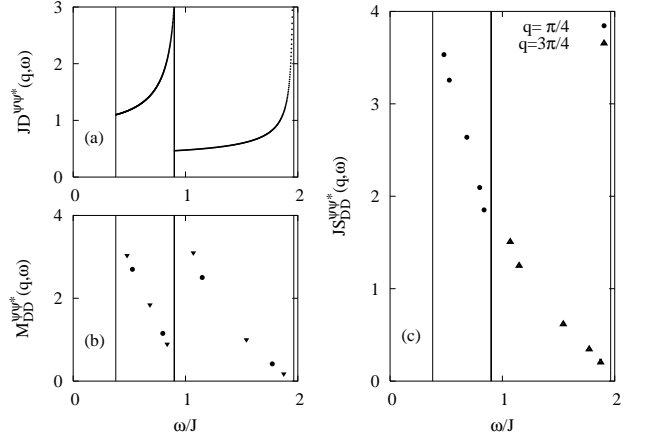


FIG. 9: (a) Density of $\psi\psi^*$ states at $q = \pi/4, 3\pi/4$ for $N = 2048$. (b) Dimer transition rates between the psinon vacuum and the $\psi\psi^*$ states at $q = \pi/4, 3\pi/4$ for $N = 16, 24$. (c) Lineshape at $q = \pi/4, 3\pi/4$ of the $\psi\psi^*$ contribution to $S_{DD}(q, \omega)$. All results are for $M_z = N/4$.

B. $S_{-+}(q, \omega)$

Here we focus on the lineshape at $q = \pi$ of the $\psi\psi$ contribution to the dynamic spin structure factor $S_{-+}(q, \omega)$. The continuum P3 of $\psi\psi$ states was previously found to be dominant. The results predicted on the basis of the product ansatz are shown in Fig. 10.

The density of states has the same characteristic shape as seen previously. The spectral weight is strongly concentrated in the lowest finite-size excitation. The scaling behavior of the transition rate for that state, $N|\langle G|S_q^-\lambda\rangle|^2 \sim (1/N)^{1/\eta-2}$, translates, via conformal

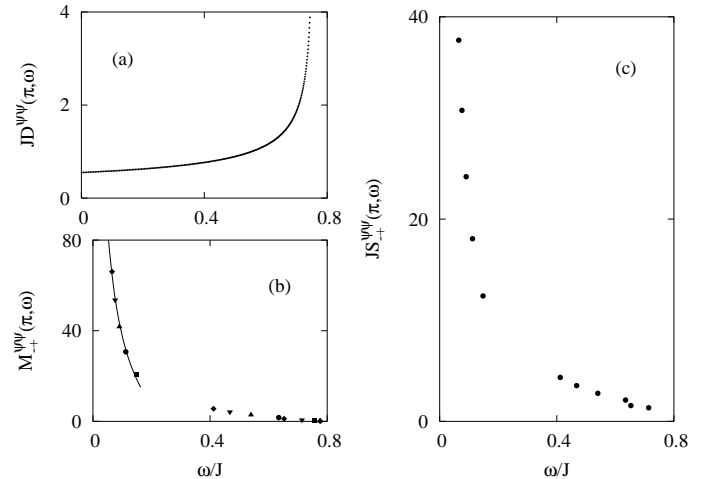


FIG. 10: (a) Density of $\psi\psi$ states at $q = \pi$ for $N = 2048$. (b) Perpendicular spin transition rates between the psinon vacuum and the $\psi\psi$ states at $q = \pi$ for $N = 12, 16, 20, 24, 28$. (c) Lineshape at $q = \pi$ of the $\psi\psi$ contribution to $S_{-+}(q, \omega)$. All results are for $M_z = N/4$.

invariance, into a power-law infrared divergence,

$$S_{-+}^{\psi\psi}(\pi, \omega) \sim \omega^{1/\eta-2}, \quad 1/\eta - 2 = -1.346 \dots, \quad (14)$$

for the spectral-weight distribution of the infinite chain. The solid line represents a two-parameter fit, $a\omega^{1/\eta-2} + b$, of the data points representing the lowest excitation for $N = 12, 16, 20, 24, 28$. The transition rate data at higher frequencies appear to approach zero sufficiently rapidly to overcome the divergent trend of the density of states to produce a monotonically decreasing spectral-weight distribution with a cusp singularity at the upper continuum boundary.

Similar single-peak lineshapes are expected for fixed- q scans across the range of the continuum P3. Hence the $\psi\psi$ contribution to the perpendicular spin fluctuations is a structure that is strongly peaked along the lower continuum boundary $\omega_L(q)$ in the shape of the psinon dispersion⁶ and a shoulder reaching to the upper boundary $\omega_U(q)$ of the continuum P2. Given the strong divergence of $S_{-+}^{\psi\psi}(q, \omega)$ at $\omega_L(q)$, the perpendicular spin fluctuations offer the most promising way to measure the energy-momentum relation of the psinon quasiparticle by means of neutron scattering.

C. $S_{+-}(q, \omega)$

Here we are back to focusing on lineshapes produced by $\psi\psi^*$ excitations as in Sec. V A, but not in the same invariant M_z subspace. Nevertheless, the continuum P6 as depicted in Fig. 7(a) produces, at $q = \pi/2$, a band of equal width and location as continuum P2 depicted in Fig. 5 did.

The data used in the product ansatz applied to $S_{+-}^{\psi\psi^*}(\pi/2, \omega)$ are shown in Fig. 11. The density of states is exactly the same as in Fig. 8. The data for the transition rates are monotonically increasing with ω . The trend in the low-frequency limit is that $M_{+-}^{\psi\psi^*}(\pi/2, \omega)$ approaches a finite value, possibly zero. Given the fact that $D^{\psi\psi^*}(\pi/2, \omega)$ is flat at low frequencies, the same trend is observed in $S_{+-}^{\psi\psi^*}(\pi/2, \omega)$. The prediction of conformal invariance for the leading infrared singularity is

$$S_{+-}^{\psi\psi^*}(\pi/2, \omega) \sim \omega^{\eta+2}, \quad \eta + 2 = 3.531 \dots \quad (15)$$

At the upper band edge ω_U , the transition rate data exhibit a pronounced maximum which could either signal a divergence or a cusp singularity for the infinite system. Whatever the case may be, this enhancement amplifies the divergent density of states in $S_{+-}^{\psi\psi^*}(\pi/2, \omega)$.

Recall that the parallel spin fluctuations exhibit a double-peak lineshape at the soft-mode wave number q_s . By contrast, the lineshape of the perpendicular spin fluctuations at the soft-mode wave number \bar{q}_s is a single-peak structure with the spectral weight concentrated near the upper band edge. For other wave numbers we do at present not have enough transitions rate data points for

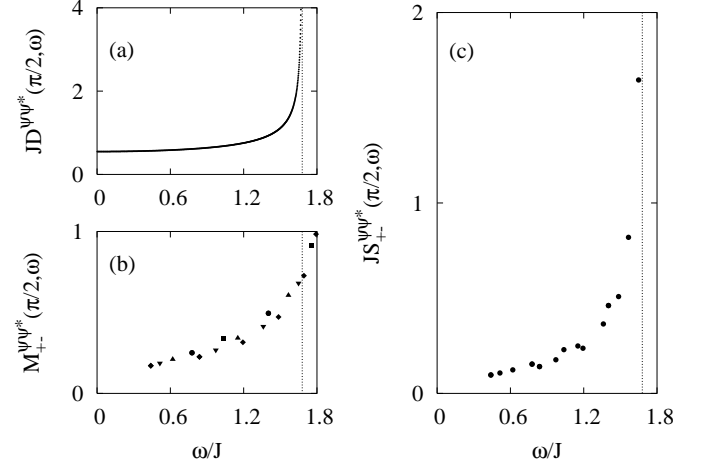


FIG. 11: (a) Density of $\psi\psi$ states at $q = \pi/2$ for $N = 2048$. (b) Perpendicular spin transition rates between the psinon vacuum and the $\psi\psi^*$ states at $q = \pi/2$ for $N = 12, 16, 20, 24, 28$. (c) Lineshape at $q = \pi/2$ of the $\psi\psi^*$ contribution to $S_{+-}(q, \omega)$. All results are for $M_z = N/4$.

a useful application of the product ansatz. Nevertheless, from the few data points which we do have some interesting conclusions can be drawn.

In the transition rate data currently available we observe that the spectral weight is heavily concentrated in a single excitation for any given $q \neq \pi/2$. For $0 \leq q < \bar{q}_s$ that excitation is located along the lower boundary of continuum P6 and for $\bar{q}_s < q \leq \pi$ along the upper boundary. Both boundaries have the shape of the antipsinon dispersion.⁶ Therefore, the contribution of $S_{+-}^{\psi\psi^*}(q, \omega)$ to the perpendicular spin fluctuations offers the most direct way to measure the dispersion of the antipsinon quasiparticle by means of neutron scattering – not once but twice, in different parts of the Brillouin zone.

The outstanding role of the excitations along the two antipsinon branches at $q < \bar{q}_s$ and $q > \bar{q}_s$ is illustrated in Fig. 12, where we have plotted the transition rates $|\langle G | S_q^+ | \lambda \rangle|^2$ versus q of all states from continuum P6 across various system sizes. However, the role of the finite- N excitations which are part of these dominant branches is different at $q < \bar{q}_s$ and $q > \bar{q}_s$. This is evident by comparison of panels (a) and (b) which show differently scaled transition rates $N^\alpha |\langle G | S_q^+ | \lambda \rangle|^2$.

To make sense of the data in this representation we must distinguish three scenarios and ask the question: For what value of the scaling exponent α do the transition rate data exhibit minimal N -dependence?

(i) For states that are inside a continuum, the product ansatz requires that the exponent $\alpha = 1$ minimizes the N -dependence of the transition rate data.

(ii) For states that mark the boundary of a continuum where the spectral-weight distribution has a divergent singularity that is not caused by a divergent density of states the exponent which minimizes the N -dependence of the transition rate data is in the range $0 < \alpha < 1$.

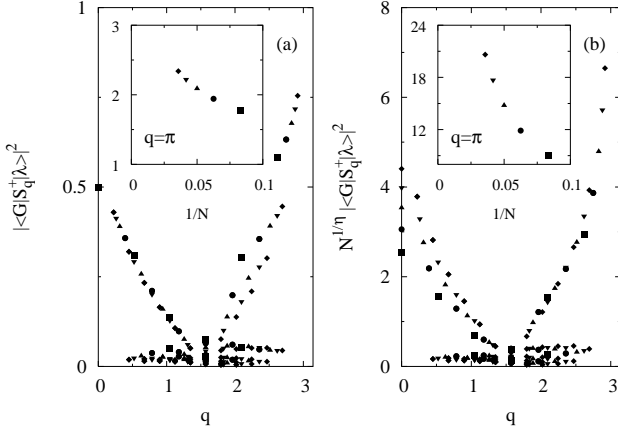


FIG. 12: (a) Unscaled and (b) scaled $\psi\psi^*$ transition rates for $S_{+-}(q, \omega)$ at $M_z = N/4$ for $N = 12, 16, 20, 24, 28$.

(iii) For states that form a branch with nonvanishing spectral weight in the limit $N \rightarrow \infty$, the exponent that minimizes the N -dependence is $\alpha = 0$.

There is ample evidence for the first scenario in the results presented earlier. The data in panel (a) strongly indicate that the third scenario is realized for the antipsinon branch at $0 < q < \bar{q}_s$. The evidence is rigorous for the isolated excitation at $q = 0$ which carries all the spectral of $S_{+-}(q, \omega)$ as discussed previously.

Panel (b) suggests that the second scenario applies to the antipsinon branch at $\bar{q}_s < q \leq \pi$. The exponent $\alpha = 1/\eta = 0.653\dots$ used here is suggested by conformal invariance, but there is a strong possibility that the singularity of $S_{+-}^{\psi\psi^*}(q, \omega)$ along the antipsinon branch at $\bar{q}_s < q \leq \pi$ is governed by a q -dependent exponent. The insets to Fig. 12 show the N -dependence of the corresponding data at $q = \pi$, which is off the scale used in the main plots. At the zone boundary, the width of continuum P6 has shrunk to zero, which is likely to affect the N -dependence of the transition rate singularly, as indicated.

In conclusion, this study makes predictions of unprecedented detail for the lineshapes of the spin and dimer fluctuations in the 1D $s = \frac{1}{2}$ Heisenberg antiferromagnet at zero temperature and nonzero magnetic field. Foremost among these predictions is the direct observability in the perpendicular spin fluctuations of the dispersion relations for the two quasiparticles which play a crucial role in this situation: the psinon and the antipsinon.

Acknowledgments

Financial support from the DFG Schwerpunkt *Kollektive Quantenzustände in elektronischen 1D Übergangsmetallverbindungen* (for M.K.) is gratefully acknowledged.

APPENDIX A: CALCULATING MATRIX ELEMENTS VIA BETHE ANSATZ

The Bethe ansatz⁴ is an exact method for the calculation of eigenvectors of integrable quantum many-body systems. The Bethe wave function of any eigenstate of (1) in the invariant subspace with $r = N/2 - M_z$ reversed spins relative to the magnon vacuum,

$$|\psi\rangle = \sum_{1 \leq n_1 < \dots < n_r \leq N} a(n_1, \dots, n_r) S_{n_1}^- \dots S_{n_r}^- |F\rangle, \quad (\text{A1})$$

has coefficients of the form

$$a(n_1, \dots, n_r) = \sum_{\mathcal{P} \in S_r} \exp \left(i \sum_{j=1}^r k_{\mathcal{P}j} n_j + \frac{i}{2} \sum_{i < j}^r \theta_{\mathcal{P}i \mathcal{P}j} \right) \quad (\text{A2})$$

determined by r magnon momenta k_i and one phase angle $\theta_{ij} = -\theta_{ji}$ for each magnon pair. The sum $\mathcal{P} \in S_r$ is over the permutations of the labels $\{1, 2, \dots, r\}$.

The consistency requirements for the coefficients $a(n_1, \dots, n_r)$ inferred from the eigenvalue equation $H|\psi\rangle = E|\psi\rangle$ and the requirements imposed by translational invariance lead to a set of coupled nonlinear equations for the k_i and θ_{ij} . A computationally convenient rendition of the Bethe ansatz equations for a state specified by Bethe quantum numbers I_1, \dots, I_r has the form

$$N\phi(z_i) = 2\pi I_i + \sum_{j \neq i} \phi[(z_i - z_j)/2], \quad i = 1, \dots, r, \quad (\text{A3})$$

where $\phi(z) \equiv 2 \arctan z$, $k_i = \pi - \phi(z_i)$ and $\theta_{ij} = \pi \operatorname{sgn}[\Re(z_i - z_j)] - \phi[(z_i - z_j)/2]$. The energy and wave number of the eigenvector thus determined are

$$\frac{E - E_F}{J} = - \sum_{i=1}^r \frac{2}{1 + z_i^2}, \quad k = \pi r - \frac{2\pi}{N} \sum_{i=1}^r I_i, \quad (\text{A4})$$

where $E_F = JN/4$ is the energy of the magnon vacuum.

In the past, The Bethe ansatz was rarely used for the purpose of calculating matrix elements. The main deterrent has been the need of evaluating the sum $\mathcal{P} \in S_r$ over the $r!$ magnon permutations in the coefficients (A2) of the Bethe eigenvectors (A1). However, the tide is now changing rapidly for two reasons: (i) the availability of vastly higher computational power, (ii) theoretical advances that make it possible to reduce matrix elements of Bethe wave functions to determinantal expressions.¹⁹

In the following, we sketch how the matrix elements can be manipulated effectively by using the Bethe wave functions directly. The use of the determinantal expressions of Bethe ansatz transition rates for the calculation of dynamic structure factors will be reported elsewhere.²⁰

In designing an efficient algorithm, we must heed the fact that in the calculation of a single matrix element,

the sum $\mathcal{P} \in S_r$ is evaluated many times, once for every coefficient $a(n_1, \dots, n_r)$ of the two eigenvectors involved. Under these circumstances, it is imperative that the algorithm has rapid access to a table of permutations. Such tables can be generated recursively by powerful algorithms.²¹

The computational effort can be reduced considerably if we use the translational symmetry of (A1), guaranteed by the relation $a(n_1 + l, \dots, n_r + l) = e^{ikl} a(n_1, \dots, n_r)$ between Bethe coefficients (A2) pertaining to basis vectors that transform into each other under translation. Translationally invariant basis vectors have the form

$$|j; k\rangle \equiv \frac{1}{\sqrt{d_j}} \sum_{l=0}^{d_j-1} e^{ilk} |j\rangle_l, \quad (\text{A5})$$

where $|j\rangle_l \equiv \mathbf{T}^l |j\rangle_0 = |n_1^{(j)} - l, \dots, n_r^{(j)} - l\rangle$ and $1 \leq N/d_j \leq N$ is an integer. The wave numbers k realized in the set (A5) are multiples mod(2π) of $2\pi/d_j$.

The set of basis vectors $|j\rangle_0 = |n_1^{(j)}, \dots, n_r^{(j)}\rangle$, $j = 1, \dots, d$, are the generators of the translationally invariant basis. The set of distinct vectors $|j; k\rangle$ for fixed k is labeled $j \in \mathcal{J}_k \subseteq \{1, \dots, d\}$. The rotationally invariant subspace for fixed $N/2 - r$, which has dimensionality $D = N!/[r!(N-r)!]$, splits into N translationally invariant subspaces of dimensionality D_k , one for each wave number $k = 2\pi n/N$, $n = 0, \dots, N-1$. We have

$$D = \sum_{j=1}^d d_j = \sum_{0 \leq k < 2\pi} D_k, \quad D_k = \sum_{j \in \mathcal{J}_k}. \quad (\text{A6})$$

The Bethe eigenvector (A1) expanded in this basis can thus be written in the form

$$|\psi\rangle = \sum_{j \in \mathcal{J}_k} a_j \sum_{l=0}^{d_j-1} e^{ilk} |j\rangle_l = \sum_{j=1}^d a_j \sum_{l=0}^{d_j-1} e^{ilk} |j\rangle_l, \quad (\text{A7})$$

where the $a_j \equiv a(n_1^{(j)}, \dots, n_r^{(j)})$, the Bethe coefficients of the generator basis vectors $|j\rangle_0$, are the only ones that must be evaluated. The last expression of (A7) holds because the Bethe coefficients a_j of all generators $|j\rangle_0$ which do not occur in the set \mathcal{J}_k are zero.

We calculate transition rates for the dynamic structure factor (2) in the form

$$|\langle G | S_q^\mu | m \rangle|^2 = \frac{|\langle \psi_0 | S_q^\mu | \psi_m \rangle|^2}{\|\psi_0\|^2 \|\psi_m\|^2}, \quad (\text{A8})$$

where $|\psi_0\rangle, |\psi_m\rangle$ are the (non-normalized) Bethe eigenvectors of the ground state and of one of the excited states from classes (i)-(vi), respectively. The norms are

$$\|\psi\|^2 = \sum_{j=1}^d d_j |a_j|^2. \quad (\text{A9})$$

The matrix element $\langle \psi_0 | S_q^\mu | \psi_m \rangle$ is nonzero only if $q = k_m - k_0 + 2\pi\mathbb{Z}$. For the fluctuation operator S_q^z it can be evaluated in the form:

$$\langle \psi_0 | S_q^z | \psi_m \rangle = \frac{1}{\sqrt{N}} \sum_{j=1}^d \bar{a}_j^{(0)} a_j^{(m)} \sum_{n=1}^N e^{iqn} \sum_{l=0}^{d_j-1} e^{ilq} \langle j | S_n^z | j \rangle_l. \quad (\text{A10})$$

The non-vanishing matrix elements $\langle \psi_0 | S_q^\pm | \psi_m \rangle$ for the other spin fluctuation operators must also satisfy $q = k_m - k_0 + 2\pi\mathbb{Z}$ and can be reduced to somewhat more complicated expressions involving elements $\langle j_0 | S_n^\pm | j_m \rangle_{l_m}$ between basis vectors from different $S_{\vec{T}}$ subspaces.

The memory requirements for the calculation of one such matrix element are 6.7MB for $N = 18, r = 9$ and 73MB for $N = 20, r = 10$.

-
- ¹ G. Müller and M. Karbach, in *Frontiers of Neutron Scattering*, edited by A. Furrer (World Scientific, Singapore, 2000), p. 168, cond-mat/0003076.
- ² V. E. Korepin, N. M. Bogoliubov, and A. G. Izergin, *Quantum Inverse Scattering Method and Correlation Functions* (Cambridge University Press, Cambridge, 1993).
- ³ C. Gómez, M. Ruiz-Altaba, and G. Sierra, *Quantum Groups in Two-Dimensional Physics* (Cambridge University Press, Cambridge, 1966).
- ⁴ H. Bethe, Z. Phys. **71**, 205 (1931).
- ⁵ L. D. Faddeev and L. A. Takhtajan, Phys. Lett. **A85**, 375 (1981).
- ⁶ M. Karbach and G. Müller, Phys. Rev. B **62**, 14871 (2000).
- ⁷ P. R. Hammar, M. B. Stone, D. H. Reich, C. Broholm, P. J. Gibson, M. M. Turnbull, C. P. Landee, and M. Oshikawa, Phys. Rev. B **59**, 1008 (1999).
- ⁸ M. Arai, M. Fujita, M. Motokawa, J. Akimitsu, and S. M.

- Bennington, Phys. Rev. Lett. **77**, 3649 (1996).
- ⁹ K. Fabricius, A. Klümper, U. Löw, B. Büchner, T. Lorenz, G. Dhaleene, and A. Revcolevschi, Phys. Rev. B **57**, 1102 (1998).
- ¹⁰ K. Fabricius and U. Löw, Phys. Rev. B **57**, 13371 (1998).
- ¹¹ The approximate nature of these additional selection rules reflects a nontrivial relationship between psinon creation operators and the physically motivated fluctuation operators. In the Haldane-Shastry model (Ref. 22), the relationship between quasiparticle creation operator and spin fluctuation operator is more direct. Here some of the additional selection rules are rigorous.
- ¹² G. Müller, H. Thomas, H. Beck, and J. C. Bonner, Phys. Rev. B **24**, 1429 (1981).
- ¹³ There is one exception to that rule. The sole excitation that contributes to $S_{+-}(0, \omega)$ is a class (v) excitation at $\omega = h$ (Ref. 12).

- ¹⁴ F. D. M. Haldane, Phys. Rev. Lett. **45**, 1358 (1980).
- ¹⁵ A. Fledderjohann, C. Gerhardt, K.-H. Mütter, A. Schmitt, and M. Karbach, Phys. Rev. B **54**, 7168 (1996).
- ¹⁶ M. Karbach, G. Müller, A. H. Bougourzi, A. Fledderjohann, and K.-H. Mütter, Phys. Rev. B **55**, 12510 (1997).
- ¹⁷ A. H. Bougourzi, M. Karbach, and G. Müller, Phys. Rev. B **57**, 11429 (1998).
- ¹⁸ M. Karbach, K. Hu, and G. Müller, Comp. in Phys. **12**, 565 (1998).
- ¹⁹ N. Kitanine, J. M. Maillet, and V. Terras, Nucl. Phys. B **554**, 647 (1999).
- ²⁰ M. Karbach, D. Biegel, and G. Müller (unpublished).
- ²¹ R. Sedgewick, *Algorithms in C++* (Addison Wesley, Reading, Massachusetts, 1992).
- ²² J. C. Talstra and F. D. M. Haldane, Phys. Rev. B **50**, 6889 (1994).